Progress In Electromagnetics Research, PIER 30, 1–32, 2001

HYBRID RAY-FDTD MOVING COORDINATE FRAME APPROACH FOR LONG RANGE TRACKING OF COLLIMATED WAVEPACKETS

Y. Pemper

Personetics, 6 Shabazi St.
Herzeliya 46370, Israel

E. Heyman and R. Kastner

Department of Electrical Engineering — Physical Electronics
Tel-Aviv University, Tel-Aviv 69978, Israel

R. W. Ziolkowski

Department of Electrical & Computer Engineering
The University of Arizona
1230 E. Speedway, Tucson, AZ 85721-0104, USA

Abstract–Modeling of long range propagation of collimated wavepackets poses some major difficulties with the conventional FDTD scheme. The difficulties arise from the vast computer resources needed to discretize the entire region of interest and the accumulation of numerical dispersion error. As a means for circumventing these difficulties, the moving frame FDTD approach is in this work. In this approach, the computational grid size is limited to the order of the pulse length, and it and moves along with the pulse. The issues discussed in conjunction with this method are those of numerical dispersion, which is shown to be reduced substantially compared with the stationary formulation, numerical stability, and absorbing boundary conditions at the leading, trailing and side boundaries, Numerical results of pulsed beam propagation in both homogeneous and plane stratified media are shown, and the capability of the method is demonstrated with propagation distances exceeding the order of 10^4 pulse lengths.

1. INTRODUCTION

This work focuses on the development of an accurate and efficient numerical approach for modeling the propagation of localized wavepackets in complex environments over large distances. Several classes of such solutions of the time-dependent wave equation have been introduced recently in linear and in nonlinear media [1–7]. The major difficulties in modeling such long distance propagation problems with an explicit, discrete numerical approach such as the conventional FDTD scheme [8–10] are the vast computer resources needed to discretize the entire region of interest and the accumulation of numerical dispersion error, which may be significant over very long propagation ranges, Furthermore, these difficulties tend to reinforce each other: while numerical dispersion can be reduced by using a finer grid, this quickly exhausts the available computer resources. Still another problem is that of numerical stability in inhomogeneous medium: trying to impose the CFL (Courant-Friedrich-Lövy) criterion globally requires a higher discretization rate than actually needed in each region separately. Considering as an example a one dimensional, inhomogeneous

medium, this condition becomes $\gamma(z) \equiv \frac{c(z)\Delta t}{\Delta z} \leq \frac{c_{\max}\Delta t}{\Delta z} \leq 1$. Thus, for a constant discretization step Δz, Δt needs to be small enough to satisfy the condition in the fastest region. This not only causes inefficient calculations, but also tends to increase numerical dispersion errors since γ becomes much smaller than unity in the slowest regions. One should also note the need for using appropriate Absorbing Boundary Conditions (ABC's) at the boundaries of the computational domain, such as the Engquist-Majda-Mur [11] and Higdon [13, 14] conditions.

The moving coordinate frame FDTD approach makes tracking of the wavepacket field over long distances feasible because (a) instead of modeling a very large computational space with a stationary coordinate frame, the numerical effort is confined to the restricted region containing the pulse, (b) the space-time trajectory for the moving frame is calculated analytical using ray techniques, and (c) numerical dispersion errors are significantly reduced since the wavespeed of the frame is found analytically. So far this approach has been studied for 1D inhomogeneous medium in [15, 16] and for 1D homogeneous, nonlinear optical medium [17]. In this paper we consider long range tracking of 3D space-time wavepackets in plane stratified media, using Pulsed Beams (PB's) [5–7] in the numerical examples, while a recent paper [18] considers the problem of wavepacket propagation in longitudinally inhomogeneous graded index media, such as optical fibers. The applications in theses two papers differ both physically and numerically. In the problem considered here, the spatial collimation of the wavepacket is due to the wavepacket structure; in [18], on the other hand, the spatial guiding is due to the graded medium (thereby introducing a temporal dispersion which becomes significant at very large distances yet is properly modeled by our moving frame FDTD scheme), Also, in the guiding medium problem the off-axis field is evanescent, whereas in the collimated wavepacket problem considered here there are no evanescent fields. This leads to a different numerical implementations, in particular for the ABC at the side walls of the moving frame.

Moving frame concepts have been used extensively in various analytical and numerical techniques in the past, however mostly in the form of the parabolic equation (PE) method or its optical counterpart, the beam propagation method (BPM) [19, 20 (Ch. 6), 22, 23]. These frequency domain methods have also been extended to the time-domain parabolic equation (TDPE) method [24, 20 (Ch. 8)]. They are based on the extraction of the rapidly varying part of the solution,

which is known analytically, resulting in an approximate, one-way (parabolic type) equation for the slowly varying term. This robust approach has been used extensively for long range tracking of wave fields in complex media. It suffers, however, from several drawbacks, as follows: The one-way approximation *a priori* precludes interactions which produce backward-propagating solutions; it assumes weak inhomogeneities; it assumes a limited propagation angle, and only scalar models are treated.

The moving frame FDTD method is free of these limitations. It is general, robust and fully vectorial, with no limitations on the medium inhomogeneity. It is not based on the one-way approximation and thus provides a full wave solution.

In this work we develop the moving frame FDTD approach for plane stratified media. The numerical examples incorporate Pulsed Beams (PB's) [5–7] as exemplars if wavepackets. In order to describe the method in the most transparent fashion, we refer to a vector acoustic equivalent of the problem which possesses fewer vector components than its electromagnetic counterpart. Yet, our moving frame FDTD approach is directly applicable to electromagnetic or other wave fields. For instance, if the p field solution presented here is considered to be the z-component of the Hertz potential, then the solver produces the Lorentz potentials from which the electromagnetic fields follow immediately with simple differentiations. The FDTD code is developed in Sec. 2. In order to reduce the computations efforts we emphasize cylindrically symmetric solutions in cylindrical coordinates (a 3D Cartezian example is considered in Sec. 5.2). The moving frame field-equations differ from the stationary frame ones in that they involve spatial as well as temporal derivatives of the same field component. Consequently, one cannot use the conventional staggered (Yee) grid formulation. Rather, we co-locate the field components at the same space-time points. A detailed numerical dispersion and stability analyses are given in Section 3. It is shown that the moving frame formulation reduces the numerical dispersion error for collimated wavepackets: In the limit where the wavepacket propagation becomes one-dimensional, numerical dispersion is inherently absent [16]. The CFL condition for the moving frame method is governed by the greatest wavespeed in the moving numerical grid, which is that of the backward propagating constituent. For a given numerical grid, the maximal time-step allowed is thus approximately half of the maximal time-step allowed in the stationary

frame formulation.

The ABCs for the moving frame scheme are developed in Section 4. The ABCs used are first-order one-way wave equations in the back (trailing) and front (leading) boundaries and a Higdon-type operator for the side boundary. Yet since the wave field is essentially stationary within the moving frame, these ABCs have certain peculiarities which are not encountered in the stationary scheme. In general, the classic, stationary-frame forms of these ABCs are formulated via two approaches, viz. the classic Engquist-Majda derivation, and the diagonalization of the original field equations into uncoupled, first-order one-way wave equations. Here we utilize the second approach and derive the ABCs for the front and back boundaries by transforming the field constituents into one-wave adiabatic constituents thus diagonalizing the field equations into weakly coupled, first-order one-way wave equations (Sec. 5.1.1). The adiabatic normalization is shown to be essential for long range tracking in inhomogeneous medium. At the back boundary we remove the incoming (forward propagating) wave constituents from the numerical grid, while at the front boundary we set the incoming (backward propagating) wave constituents to zero. The ABC for the side boundary is obtained in Sec. 5.1.2 by transforming the stationary frame, Higdon-type operator into the moving frame formulation, and the corner points are discussed in Sec. 5.1.3 Numerical examples are given in Section 5 for cylindrically symmetric pulsed beams in free space (Section 5.1) and in plane stratified medium (Section 5.2). The results are compared to known exact and approximate solutions, and the effects of the computational domain size with relation to the ABC's are discussed. Finally, conclusions are drawn in Section 6.

2. THE MOVING COORDINATE FRAME FDTD CODE

2.1 Field Equations

As has been mentioned in the introduction, we present the moving frame FDTD the context of the vector acoustic field in the simplest most transparent fashion. Yet the analysis does not utilize any special property of the acoustic field, and the results are immediately applicable to the vector electromagnetic case. We consider the acoustic wave equations

$$\partial_t \mathbf{v} = -\frac{1}{\rho}\nabla p, \qquad \partial_t p = -c^2 \rho \nabla \cdot \mathbf{v}, \tag{1}$$

where p is the pressure, $\mathbf{v}$ is the particle velocity vector, $\rho = \rho(\mathbf{x})$ and $c = c(\mathbf{x})$ are the density and sound speed of the medium, respectively; $\mathbf{x} = (x, y, z)$ denotes the position in a 3D coordinate frame and boldface is used to denote vectors. Henceforth we shall assume that the medium is plane stratified along the z axis with $c = c(z)$, while $\rho = 1$.

2.2 Moving Coordinate Frame Formulation

We shall consider wave configurations where the wavepacket propagates parallel to the z-axis at some wavespeed $c^w(z)$, and shall track the field in a frame that moves at this speed. Therefore, we introduce a moving coordinate frame ζ, defined by:

$$\zeta = \int_0^z \frac{c_0}{c^w(z')} dz' - c_0 t, \tag{2}$$

where c_0 is an arbitrary reference velocity. The integral in (2) defines the optical path length that maps the z axis onto an equi-propagation-time axis. Subtracting $c_0 t$ describes ζ as an optical coordinate centered about the wavepacket's center of mass.

Examples for this transformation are: (a) A plane stratified medium with a wave propagating along the stratification axis, giving $c^w(z) = c(z)$. (b) Same as above, but with a dispersive medium $c = c(z, \omega)$. For this type of problem one may choose $c^w(z) = c(z, \omega_0)$ where ω_0 is the center frequency of the pulse (this example is not treated in this paper). (c) A graded index waveguiding structure (e.g., an optical fiber) with the general form $c(z, r) = \bar{c}(z)/\bar{n}(z, r)$, $r = \sqrt{x^2 + y^2}$, where the profile function $\bar{n}(z, r)$ is monotonously decreasing away from the z axis with $\bar{n}(0, r) = 1$, so that $\bar{c}(z)$ is the wavespeed on the axis. Since the modal propagation speed is close to $\bar{c}(z)$, we choose here $c^w(z) = \bar{c}(z)$ (see [18]).

2.3 Plane Stratified Medium — Field Equations

In this paper we shall only consider the case of wavepacket propagation in a plane stratified medium with $c = c(z)$. We shall transform the field equations to the moving frame and denote

$$\mathbf{v}(x, y, z, t) = \hat{\mathbf{z}} V(x, y, \zeta, t) + \mathbf{U}(x, y, \zeta, t), \quad \text{where} \quad \mathbf{U} \cdot \hat{\mathbf{z}} = 0 \tag{3a}$$

$$p(x, y, z, t) = P(x, y, \zeta, t), \tag{3b}$$

where here and henceforth we use a caret to denote unit vectors. For mathematical convenience we have also separated the longitudinal and transversal components of the particle velocity vector, denoting them as V and $\mathbf{U}$, respectively. Using (2), with $c^w(z) = c(z)$, the field equations (1) become:

$$\partial_t V = c_0 \partial_\zeta V - \frac{c_0}{\tilde{c}} \partial_\zeta P \tag{4a}$$

$$\partial_t \mathbf{U} = c_0 \partial_\zeta \mathbf{U} - \nabla_t P \tag{4b}$$

$$\partial_t P = c_0 \partial_\zeta P - c_0 \tilde{c} \partial_\zeta V - \tilde{c}^2 \nabla_t \cdot \mathbf{U}, \tag{4c}$$

where $\nabla_t = \hat{\mathbf{x}}\partial_x + \hat{\mathbf{y}}\partial_y$ and $\tilde{c}(\zeta, t) = c[z(\zeta, t)]$.

In this article we shall mainly consider cylindrically symmetric wave solutions which reduce the computational efforts. The analysis of the cylindrically symmetric code that will be carried out is straightforwardly extensible to the general cartesian coordinate case. We have also formulated the full cartesian coordinate coordinate code, and its numerical results will be presented below.

For the cylindrically symmetric case we denote $\mathbf{U} = \hat{\mathbf{r}} U$, bringing (4) to the form

$$\partial_t V = c_0 \partial_\zeta V - \frac{c_0}{\tilde{c}} \partial_\zeta P \tag{5a}$$

$$\partial_t U = c_0 \partial_\zeta U - \partial_r P \tag{5b}$$

$$\partial_t P = c_0 \partial_\zeta P - c_0 \tilde{c} \partial_\zeta V - \tilde{c}^2 \frac{1}{r} \partial_r (rU), \tag{5c}$$

with the axial boundary conditions $\partial_r P = \partial_r V = U = 0$ at $r = 0$.

The central-difference discretized form of (5), organized in a "marching in time" form, is thus:

$$V_{i,j}^{n+1} = V_{i,j}^{n-1} + \gamma_\zeta \left(V_{i+1,j}^n - V_{i-1,j}^n \right) - (\gamma_\zeta / \tilde{c}_i^n) \left(P_{i+1,j}^n - P_{i-1,j}^n \right) \tag{6a}$$

$$U_{i,j}^{n+1} = U_{i,j}^{n-1} + \gamma_\zeta \left(U_{i+1,j}^n - U_{i-1,j}^n \right) - \gamma_r c_0^{-1} \left(P_{i,j+1}^n - P_{i,j-1}^n \right) \tag{6b}$$

$$\begin{aligned} P_{i,j}^{n+1} = {} & P_{i,j}^{n-1} + \gamma_\zeta \left(P_{i+1,j}^n - P_{i-1,j}^n \right) - \tilde{c}_i^n \gamma_\zeta \left(V_{i+1,j}^n - V_{i-1,j}^n \right) \\ & - (\tilde{c}_i^n)^2 {c_0}^{-1} \gamma_r \frac{1}{r_j} \left(r_{j+1} U_{i,j+1}^n - r_{j-1} U_{i,j-1}^n \right) \end{aligned} \tag{6c}$$

The problem space is discretized uniformly: t, ζ, and r are sampled uniformly at the points $t_n = n\Delta t$, $\zeta_i = i\Delta\zeta$, $r_j = j\Delta r$, where $i =$

$0, 1, \ldots, I$ and $j = 0, 1, \ldots, J$ [8]. We denote $\gamma_\zeta = \frac{c_0 \Delta t}{\Delta \zeta}$, $\gamma_r = \frac{c_0 \Delta t}{\Delta r}$ and $\tilde{c}_i^n = \tilde{c}(i\Delta\zeta,\ n\Delta t)$.

Treatment of the Axial Singularity

Eq. (6a) applies for $j \geq 0$, while (6b) and (6c) apply for $j \geq 1$. In (6b) we have $U = 0$ for $j = 0$. The singularity of (6c) at $r = 0$ is addressed by integrating (5c) within the elementary volume $dv = 2\pi r dr d\zeta$ around the $r = 0$ axis, yielding, using the divergence theorem:

$$\int_0^{\Delta r} r dr \left[\partial_t P - c_0(\partial_\zeta P - \tilde{c}\partial_\zeta V)\right] = -\tilde{c}^2 [rU]_{r=\Delta r}. \tag{7}$$

Integrating by parts the integral on the left hand side yields

$$\frac{1}{2}(\Delta r)^2 \left[\partial_t P - c_0(\partial_\zeta P - \tilde{c}\partial_\zeta V)\right] - \int_0^{\Delta r} dr \frac{1}{2} r^2 \partial_r \left[\partial_t P - c_0(\partial_\zeta P - \tilde{c}\partial_\zeta V)\right] \tag{8}$$

In view of the axial boundary conditions mentioned after (5), the integral in (8) is $\mathcal{O}((\Delta r)^4)$ and may therefore be neglected. Substituting in (7) yields

$$\partial_t P|_{r=0} = c_0 \partial_\zeta P|_{r=0} - c_0 \tilde{c} \partial_\zeta V|_{r=0} - \frac{2}{\Delta r} \tilde{c}^2 U \Big|_{r=\Delta r} + \mathcal{O}\left((\Delta r)^2\right) \tag{9}$$

or, in central-difference form:

$$\begin{aligned} P_{i,0}^{n+1} = P_{i,0}^{n-1} &+ \gamma_\zeta \left(P_{i+1,0}^n - P_{i-1,0}^n\right) - \tilde{c}_i^n \gamma_\zeta \left(V_{i+1,0}^n - V_{i-1,0}^n\right) \\ &- 4(\tilde{c}_i^n)^2 {c_0}^{-1} \gamma_r U_{i,1}^n. \end{aligned} \tag{10}$$

This equation replaces (6c) for $j = 0$.

3. DISPERSION AND STABILITY ANALYSIS

3.1 Dispersion Analysis

In order to derive the numerical dispersion relation, we may assume in the analysis that the medium is locally uniform, with constant sound velocity c. We make an ansatz for a space-time harmonic solution of the following form:

$$\begin{pmatrix} V_{i,j}^n \\ U_{i,j}^n \\ P_{i,j}^n \end{pmatrix} = \begin{pmatrix} V_0 J_0(k_r r_j) \\ U_0 J_1(k_r r_j) \\ P_0 J_0(k_r r_j) \end{pmatrix} e^{-\imath[\omega t_n - k_\zeta \zeta_i]} \tag{11}$$

where k_r and k_ζ are wave numbers; J_0 and J_1 are Bessel functions of the zero and first order, respectively, and $\imath = \sqrt{-1}$ should not be confused with the subscript i. Substituting into (6), we obtain the matrix equation

$$\begin{pmatrix} \sin\Omega + \gamma_\zeta \sin K_\zeta & 0 & -\gamma_\zeta c^{-1} \sin K_\zeta \\ 0 & \sin\Omega + \gamma_\zeta \sin K_\zeta & -\imath\gamma_r c_0^{-1} K_r \\ -\gamma_\zeta c \sin K_\zeta & \imath\gamma_r c^2 c_0^{-1} K_r & \sin\Omega + \gamma_\zeta \sin K_\zeta \end{pmatrix} \begin{pmatrix} V_0 \\ U_0 \\ P_0 \end{pmatrix} = 0 \tag{12}$$

where $K_\zeta = k_\zeta \Delta\zeta$, $K_r = k_r \Delta r$, and $\Omega = \omega \Delta t$. In this derivation we have used the relations $2k_r \Delta r J'_n(k_r r_j) \approx J_n(k_r r_{j+1}) - J_n(k_r r_{j-1})$, $J'_0(z) = -J_1(z)$ and $\{zJ_1(z)\}' = zJ_0(z)$. The local numerical dispersion relation is described by the zeros of the determinant:

$$\sin\Omega + \gamma_\zeta \sin K_\zeta = 0 \tag{13a}$$

$$(\sin\Omega + \gamma_\zeta \sin K_\zeta)^2 - \gamma_\zeta^2 \sin^2 K_\zeta - \frac{c^2}{c_0^2}\gamma_r^2 K_r^2 = 0 \tag{13b}$$

Eq. (13a) describes backward propagation in the moving frame. In particular for small Ω and K_ζ it reads

$$v_p = \frac{\omega}{k_\zeta} \approx -c_0 \left[1 + \mathcal{O}\left(\Omega^2, K_\zeta^2\right)\right] \tag{14}$$

where v_p denotes the phase velocity. This phase velocity in the moving frame corresponds to the radial propagation of U in the stationary frame.

Eq. (13b) is rewritten as

$$\begin{aligned} \sin\Omega + \gamma_\zeta \sin K_\zeta &= \pm\gamma_\zeta \sin K_\zeta \sqrt{1 + \frac{c^2\gamma_r^2}{c_0^2\gamma_\zeta^2}\frac{K_r^2}{\sin^2 K_\zeta}} \\ &\approx \pm\gamma_\zeta \sin K_\zeta \sqrt{1 + \frac{c^2 k_r^2}{c_0^2 k_\zeta^2}}, \end{aligned} \tag{15}$$

where in the approximation we have used $\sin K_\zeta \approx K_\zeta$. We shall estimate the resulting numerical dispersion assuming an excitation by a collimated PB with [1]

$$(k_r/k_\zeta)^2 \equiv \epsilon \ll 1. \tag{16}$$

Using (16), (15) reduces to

$$\sin\Omega + \gamma_\zeta \sin K_\zeta \approx \pm\gamma_\zeta \sin K_\zeta \left(1 + \frac{c^2}{c_0^2}\frac{\epsilon}{2}\right). \tag{17}$$

This equation has two possible solutions: Taking the upper sign it yields

$$\sin\Omega \approx \frac{c^2}{c_0^2}\frac{\epsilon}{2}\gamma_\zeta \sin K_\zeta. \tag{18}$$

This almost stationary solution corresponds to the forward propagating spectrum in the stationary frame. Indeed, in the 1D limit (a pulsed plane wave propagating along the z axis) we have $k_r = 0$ giving $\epsilon = 0$ and thus $\sin\Omega = 0$ and $v_g = v_p = 0$, where v_g designate the group velocity in the moving frame. This solution implies that the moving-coordinate frame formulation in the 1D limit is free of numerical dispersion errors regardless of the discretization ratio γ_ζ [15, 16]. For small Ω and K_ζ (18) yields

$$v_p = \frac{\omega}{k_\zeta} \approx \frac{c^2}{c_0}\frac{\epsilon}{2}\left[1 + \mathcal{O}\left(\Omega^2, K_\zeta^2\right)\right] \ll \frac{c^2}{c_0}, \tag{19}$$

hence to leading order, the numerical dispersion is independent of the discretization, however it does depend on ϵ (the spectral content of the wavepacket), and disappears in the plane-wave limit $\epsilon \to 0$. To find the group velocity in the ζ direction we rewrite (19) as $\omega \approx \frac{1}{2}\frac{c^2}{c_0}\frac{k_r^2}{k_\zeta}$, hence

$$v_g = \frac{\partial\omega}{\partial k_\zeta} \approx -\frac{1}{2}\frac{c^2}{c_0}\frac{k_r^2}{k_\zeta^2} = -\frac{c^2}{c_0}\frac{\epsilon}{2}. \tag{20}$$

[1] For example, the class of collimated PBs considered in [5] and [7] (to be utilized in the numerical examples in Section 5.1 below) satisfies the spectral estimates: $k_r \sim \mathcal{O}(W_0^{-1}) \sim \mathcal{O}\left((c_0 T b)^{-1/2}\right)$ and $k_\zeta \sim \mathcal{O}\left((c_0 T)^{-1}\right)$ where T is the temporal pulse length, b is the collimation distance and $W_0 = \sqrt{c_0 T b}$ is the beam width at the PB waist. These PBs are collimated if $c_0 T/b \ll 1$, thus giving $(k_r/k_\zeta)^2 \sim \mathcal{O}(c_0 T/b) \ll 1$.

Taking next the lower sign in (17) we obtain

$$\sin\Omega \approx -\gamma_\zeta \left(2 + \frac{c^2}{c_0^2}\frac{\epsilon}{2}\right) \sin K_\zeta, \tag{21}$$

giving, for small Ω and K_ζ,

$$v_p = \frac{\omega}{k_\zeta} \approx -2c_0 \left(1 + \frac{c^2}{c_0^2}\frac{\epsilon}{4}\right) \left[1 + \mathcal{O}\left(\Omega, K_\zeta^2\right)\right] \approx -2c_0. \tag{22}$$

Clearly this solution corresponds to the backward propagating wave in the stationary frame.

Dispersion Relation in the Continuous Domain Case

To further understand the numerical dispersion relations, we shall show that in the limit of small Ω and K_ζ they tend to the continuous dispersion relation for a moving coordinate frame. To compute the later we resort first to the stationary frame where the cylindrically symmetric eigenfunctions are

$$\begin{pmatrix} V \\ U \\ P \end{pmatrix} = \begin{pmatrix} V_0 J_0(k_r r) \\ U_0 J_1(k_r r) \\ P_0 J_0(k_r r) \end{pmatrix} e^{-\imath[\tilde{\omega}t - k_z z]}, \tag{23}$$

where $\tilde{\omega}$, k_r, and k_z designate the frequency and wave numbers in the r and z directions, respectively, in the stationary frame. The dispersion relation in of these solutions is

$$k_r^2 + k_z^2 = \tilde{\omega}^2/c^2, \tag{24}$$

where c designates, as in the numerical dispersion formulation, the wave speed in the (locally) uniform medium.

In order to transform this dispersion relation to the moving frame we note that under the assumption of a uniform medium, (2) yields $\zeta = c_0(z/c - t)$. Thus, since the transformation to the moving frame involves only the z coordinate, we find that the eigenfunctions in (23) are valid also in the moving frame provided that the term $e^{-\imath[\tilde{\omega}t - k_z z]}$ therein is replaced by $e^{-\imath[(\tilde{\omega} - k_z c)t - \frac{c}{c_0}k_z \zeta]}$. We thus identify the frequency and the ζ direction wave number in the moving frame $\omega = \tilde{\omega} - k_z c$ and $k_\zeta = \frac{c}{c_0}k_z$. Substituting into (24) we obtain

$$\omega^2 + 2\omega k_\zeta c_0 - c^2 k_r^2 = 0, \tag{25}$$

with the solution

$$\omega + c_0 k_\zeta = \pm c_0 k_\zeta \sqrt{1 + \frac{c^2 k_r^2}{c_0^2 k_\zeta^2}} \approx \pm c_0 k_\zeta \left(1 + \frac{c^2}{c_0^2}\frac{\epsilon}{2}\right), \tag{26}$$

where ϵ is defined in (16). Form (26) we obtain

$$\frac{\omega}{k_\zeta} \approx \frac{c^2}{c_0}\frac{\epsilon}{2}, \quad \frac{\omega}{k_\zeta} \approx -2c_0\left(1 + \frac{c^2}{c_0^2}\frac{\epsilon}{4}\right). \tag{27}$$

The first and second expressions in (27) correspond to the leading order terms in (19) and (22), respectively, showing, as expected, that the moving frame numerical dispersion relations for collimated PBs recover the continuous frame relations in the limit $\Omega,\ K_\zeta \to 0$.

3.2 Numerical Stability

In general, the stability condition is implicitly contained in the numerical dispersion relations. The space-time harmonic ansatz (11) has a time increment dependency of $e^{-\imath\omega tn} = e^{-\imath\Omega n}$. Thus, deriving the stability condition is tantamount to substituting $g = e^{-\imath\Omega}$ into the numerical dispersion relations and demanding that

$$gg^* \le 1 \quad \forall \text{ real } K_\zeta,\ K_r. \tag{28}$$

Thus Eq. (13) gives

$$g^{-1} - g + \imath 2\gamma_\zeta \sin K_\zeta = 0 \tag{29a}$$

$$\left(g^{-1} - g + \imath 2\gamma_\zeta \sin K_\zeta\right)^2 + 4(c/c_0)^2\gamma_r^2 K_r^2 + 4\gamma_\zeta^2 \sin^2 K_\zeta = 0. \tag{29b}$$

Eq. (29a) yields $g = \imath\gamma_\zeta \sin K_\zeta \pm \sqrt{1 - \gamma_\zeta^2 \sin^2 K_\zeta}$, hence the stability condition (28) is satisfied $\forall$ real K_ζ if and only if

$$\gamma_\zeta \le 1, \qquad (\text{i.e., } c_0\Delta t \le \Delta\zeta). \tag{30}$$

Note that in this case $|g| = 1$.

Eq. (29b) gives

$$g^{-1} - g + \imath 2\gamma_\zeta \sin K_\zeta \approx \pm\imath 2\gamma_\zeta \sin K_\zeta \sqrt{1 + (c/c_0)^2\epsilon} \tag{31}$$

where we used the same approximation as in (15). For collimated pulses, the correction term inside the square root is small and may be approximated to first order. We obtain the following equation

$$g^2 - \imath 2 g \gamma_\zeta \sin K_\zeta \left(1 \pm \left(1 + \frac{1}{2}(c/c_0)^2 \epsilon\right)\right) - 1 = 0 \qquad (32)$$

Noting from this equation that $|g_1|\,|g_2| = 1$, the stability condition (28) is satisfied if and only if $|g_1| = |g_2| = 1,\ \forall K_z,\ K_r$. This implies

$$\left|\gamma_\zeta \left(1 \pm \left(1 + \frac{1}{2}(c/c_0)^2 \epsilon\right)\right) \sin K_\zeta\right| \le \gamma_\zeta \left|1 \pm \left(1 + \frac{1}{2}(c/c_0)^2 \epsilon\right)\right| \le 1 \qquad (33)$$

Thus, taking the upper sign in (33) we obtain

$$\gamma_\zeta \le \frac{1}{2}\left(1 - \frac{1}{4}(c/c_0)^2 \epsilon\right) \approx \frac{1}{2}, \qquad \left(\text{i.e., } c_0 \Delta t \le \frac{1}{2}\Delta\zeta\right), \qquad (34)$$

where the small correction term has been neglected for $\epsilon \ll 1$. The stability condition (34) is stronger than the previous one and therefore will be used throughout. It is the analog of the CFL condition in the stationary coordinate frame, recalling that in the moving coordinate frame the greatest wave speed is $2c_0$ (for the backward propagating wave).

Finally, taking the lower sign in (33) we obtain the stability condition

$$\gamma_\zeta \le 2(c/c_0)^2 \epsilon^{-1}. \qquad (35)$$

Since $\epsilon \ll 1$ this condition is much weaker than the CFL condition (34).

4. ABSORBING BOUNDARY CONDITIONS

In this section, the formulation of boundary conditions for the moving coordinate frame (2) will be addressed. Our formulation is second order accurate. We implement first order boundary conditions that adapt themselves continuously to the local changes in the medium properties. This provides a stable and accurate scheme over very large distances. We assume, without loss of generality, that our grid is located in the region $0 \le \zeta \le \zeta_{\max}$ and $0 \le r \le r_{\max}$.

4.1 Adaptive ABCs for the Back and Front Boundaries

In general, when considering first order boundary condition schemes, it is necessary to analyze the field components propagating in the direction normal to the boundary at hand. Consequently, when considering the back boundary $\zeta = 0$ and the front boundary $\zeta = \zeta_{\max}$, we assume $\partial_r = 0$ in (5), obtaining:

$$\partial_t V = c_0 \partial_\zeta V - \frac{c_0}{\tilde{c}} \partial_\zeta P \tag{36a}$$

$$\partial_t U = c_0 \partial_\zeta U \tag{36b}$$

$$\partial_t P = c_0 \partial_\zeta P - c_0 \tilde{c} \partial_\zeta V. \tag{36c}$$

In order to develop the adaptive ABCs that accommodate the variations of $c(z)$, we transform the relevant field constituents to adiabatic-type constituents using

$$\tilde{P} = \tilde{c}^{-1/2} P, \qquad \tilde{V} = \tilde{c}^{1/2} V. \tag{37}$$

We thus have for (36a) and (36c)

$$\partial_t \tilde{V} = c_0 \partial_\zeta \tilde{V} - c_0 \partial_\zeta \tilde{P} - \frac{1}{2} c_0 \frac{\partial_\zeta \tilde{c}}{\tilde{c}} \tilde{P} \tag{38a}$$

$$\partial_t \tilde{P} = c_0 \partial_\zeta \tilde{P} - c_0 \partial_\zeta \tilde{V} + \frac{1}{2} c_0 \frac{\partial_\zeta \tilde{c}}{\tilde{c}} \tilde{V}. \tag{38b}$$

In deriving (38) we also note that c is t-independent, so that $(\partial_t - c_0 \partial_\zeta)\tilde{c} = 0$. By adding and subtracting (38a) and (38b) we obtain

$$\partial_t \overset{+}{W} = -\frac{1}{2} c_0 \frac{\partial_\zeta \tilde{c}}{\tilde{c}} \overset{-}{W} \tag{39a}$$

$$\partial_t \overset{-}{W} = 2 c_0 \partial_\zeta \overset{-}{W} + \frac{1}{2} c_0 \frac{\partial_\zeta \tilde{c}}{\tilde{c}} \overset{+}{W}, \tag{39b}$$

where

$$\overset{\pm}{W} = \tilde{P} \pm \tilde{V} = \tilde{c}^{-1/2} P \pm \tilde{c}^{1/2} V \tag{40}$$

are henceforth identified as the "one-way wave constituents" (Fig. 1).

Neglecting the coupling terms in (39), we finally obtain the diagonalized system of equations

$$\partial_t \overset{+}{W} = 0 \tag{41a}$$

$$\partial_t \overset{-}{W} = 2 c_0 \partial_\zeta \overset{-}{W} \tag{41b}$$

$$\partial_t U = c_0 \partial_\zeta U. \tag{41c}$$

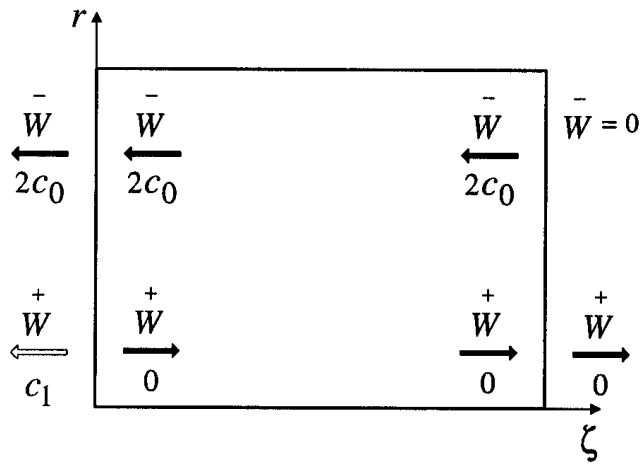

Figure 1. One-way wave constituents in the moving frame. The rectangle represents the boundary of the numerical grid. The solid arrows inside the numerical grid represent the one-way wave constituents and the corresponding *physical* one-way wave equations which (in the form of propagation speed and direction). The arrows outside the numerical grid represent the *numerical* boundary conditions (i.e., the one way wave equations) imposed on these constituents: The empty arrow indicates the *artificial* boundary condition used to remove the reflected one-way wave constituent $\overset{+}{W}$ from the back boundary of the numerical grid. At the front boundary we set $\overset{-}{W} = 0$.

Thus $\overset{+}{W}$, $\overset{-}{W}$ and U satisfy first-order one-way wave equations and propagate at velocities 0, $-2c_0$ and $-c_0$, respectively, in the ζ direction.

(A) ABCs for the Back Boundary

At the back boundary $\zeta = 0$, $\overset{-}{W}$ and U exit the computational grid, while $\overset{+}{W}$ is stationary. With respect to that boundary, $\overset{-}{W}$ is the incident one-way wave constituent and $\overset{+}{W}$ is the reflected one-way wave constituent that should be absorbed. This reflected one-way wave constituent is stationary and does not propagate into the problem space, yet, if untreated, it accumulates on the back boundary. To remedy this situation we employ an outgoing one-way wave equation

which removes $\overset{+}{W}$ from the problem space:

$$\partial_t \overset{+}{W} = c_1 \partial_\zeta \overset{+}{W}; \qquad c_1 > 0, \tag{42}$$

where c_1 is an arbitrary velocity which must be large enough to effectively remove the reflected one-way wave constituent from the problem space. For $\overset{-}{W}$ we must use (41b) because of continuity considerations (numerical tests show that changing the velocity $2c_0$ in (41b) to a different velocity causes numerical instability, as can be expected). For U we shall use the one-way wave equation (41c). These ABC are summarized in Fig. 1.

Numerical implementation of the continuous boundary conditions is obtained using the Mur finite-difference scheme [12]:

$$\overset{+}{W}{}^{n+1}_{0,j} = \overset{+}{W}{}^{n}_{1,j} + \frac{c_1\Delta t - \Delta\zeta}{c_1\Delta t + \Delta\zeta}\left(\overset{+}{W}{}^{n+1}_{1,j} - \overset{+}{W}{}^{n}_{0,j}\right) \tag{43a}$$

$$\overset{-}{W}{}^{n+1}_{0,j} = \overset{-}{W}{}^{n}_{1,j} + \frac{2c_0\Delta t - \Delta\zeta}{2c_0\Delta t + \Delta\zeta}\left(\overset{-}{W}{}^{n+1}_{1,j} - \overset{-}{W}{}^{n}_{0,j}\right) \tag{43b}$$

$$U^{n+1}_{0,j} = U^{n}_{1,j} + \frac{c_0\Delta t - \Delta\zeta}{c_0\Delta t + \Delta\zeta}\left(U^{n+1}_{1,j} - U^{n}_{0,j}\right) \tag{43c}$$

Finally the field constituents are given by

$$V^{n+1}_{0,j} = \frac{1}{2}\left[\tilde{c}^{n+1}_0\right]^{-1/2}\left(\overset{+}{W}{}^{n+1}_{0,j} - \overset{+}{W}{}^{n+1}_{0,j}\right) \tag{44a}$$

$$P^{n+1}_{0,j} = \frac{1}{2}\left[\tilde{c}^{n+1}_0\right]^{1/2}\left(\overset{+}{W}{}^{n+1}_{0,j} + \overset{+}{W}{}^{n+1}_{0,j}\right). \tag{44b}$$

In Section 5.1.4 we present numerical results for different values of c_1. Form these results it is evident that the value of c_1 controls the speed at which the reflected component $\overset{-}{W}$ is removed from the computational grid. A value of $c_1/c_0 = 10^{-1}$ is sufficiently large to remove any trace of the reflected one-way wave constituent. Any higher values give the same result. Thus, since the choice of c_1 is arbitrary, we may choose $c_1 = 2c_0$, which provides simpler expressions. In this case, combining (41b) with (42) yields

$$\partial_t \tilde{c}^{1/2} V = 2c_0 \partial_\zeta \tilde{c}^{1/2} V \tag{45a}$$

$$\partial_t \tilde{c}^{-1/2} P = 2c_0 \partial_\zeta \tilde{c}^{-1/2} P. \tag{45b}$$

Eqs. (45) are readily discretized as:

$$V_{0,j}^{n+1} = \frac{1}{\sqrt{\tilde{c}_0^{n+1}}}\left[\sqrt{\tilde{c}_1^{n}}V_{1,j}^{n} + \frac{2c_0\Delta t - \Delta\zeta}{2c_0\Delta t + \Delta\zeta}\left(\sqrt{\tilde{c}_1^{n+1}}V_{1,j}^{n+1} - \sqrt{\tilde{c}_0^{n}}V_{0,j}^{n}\right)\right] \quad (46a)$$

$$P_{0,j}^{n+1} = \sqrt{\tilde{c}_0^{n+1}}\left[\frac{P_{1,j}^{n}}{\sqrt{\tilde{c}_1^{n}}} + \frac{2c_0\Delta t - \Delta\zeta}{2c_0\Delta t + \Delta\zeta}\left(\frac{P_{1,j}^{n+1}}{\sqrt{\tilde{c}_1^{n+1}}} - \frac{P_{0,j}^{n}}{\sqrt{\tilde{c}_0^{n}}}\right)\right]. \quad (46b)$$

These equation are also obtained by combining (40), (43) and (44) and setting $c_1 = 2c_0$.

(B) ABCs for the Front Boundary

At the front boundary $\zeta = \zeta_{\max}$, $\bar{W}$ and U enter the grid from the outside. The one-way constituent $\overset{+}{W}$ is stationary and never impinges upon the front boundary, so that there is no numerical reflection at the front boundary. Therefore, we cannot remove $\bar{W}$ and U from the problem space as we did with $\overset{+}{W}$ at the back boundary. Numerical tests show that attempting to remove $\bar{W}$ or U from the problem space causes numerical instability at any removal speed (i.e., c_1) we choose (furthermore, in [18] we show that this instability occurs also for the case where $\overset{+}{W}$ is not stationary and does impinge upon the front boundary). Thus, the solution is to specify $\bar{W}$ and U on the front boundary according to our knowledge of their behavior. For $\bar{W}$ we utilize the fact that the moving frame is moving at the local wavespeed. Choosing the initial frame so that there is no field ahead of the front boundary, one can force the field exterior to that boundary to vanish for all $t > 0$ and, hence, we may set there

$$\bar{W}\,|_{\zeta=\zeta_{\max}} = 0. \quad (47)$$

The same condition also applies for $U = V_r$. Finally, for $\overset{+}{W}$ we use (41a), because of continuity considerations (as before). If, however, the basic assumption of vanishing fields ahead of the front boundary is not satisfied in the physical realm, we may expect error accumulation near the front boundary (see the numerical study in Sec. 5.1.3).

Numerical implementation of these boundary conditions with $i = I$ is readily obtained:

$$\overset{+}{W}{}^{n+1}_{I,j} = \overset{+}{W}{}^{n}_{I,j} \tag{48a}$$

$$\overset{-}{W}{}^{n+1}_{I,j} = 0 \tag{48b}$$

$$U^{n+1}_{I,j} = 0, \tag{48c}$$

and finally, in the field constituents

$$V^{n+1}_{I,j} = \frac{1}{2\sqrt{\tilde{c}^{n+1}_I}} \left(\overset{+}{W}{}^{n+1}_{I,j} - \overset{-}{W}{}^{n+1}_{I,j} \right) = \frac{1}{2\sqrt{\tilde{c}^{n+1}_I}} \left(\frac{P^n_{I,j}}{\sqrt{\tilde{c}^n_I}} + \sqrt{\tilde{c}^n_I} V^n_{I,j} \right) \tag{49a}$$

$$P^{n+1}_{I,j} = \frac{\sqrt{\tilde{c}^{n+1}_I}}{2} \left(\overset{+}{W}{}^{n+1}_{I,j} + \overset{-}{W}{}^{n+1}_{I,j} \right) = \frac{\sqrt{\tilde{c}^{n+1}_I}}{2} \left(\frac{P^n_{I,j}}{\sqrt{\tilde{c}^n_I}} + \sqrt{\tilde{c}^n_I} V^n_{I,j} \right). \tag{49b}$$

4.2 Higdon-Type Operator for the Side Boundary

The boundary condition for the side boundary $r = r_{\max} = J\Delta r$ will be derived under the assumption that we are dealing with a collimated PB whose spectral constituents propagate at an angle $\theta \ll 1$ relative to the ζ axis. A higdon-type annihilation operator for the $r = r_{\max}$ boundary in a stationary coordinate frame is given by $(\sin\theta\partial_t + c\partial_r)W = 0$. Transformation to the moving frame yields:

$$\left[\sin\theta(\partial_t + c_0\partial_\zeta) + c\partial_r\right] W = 0. \tag{50}$$

Since $\theta \ll 1$ we may neglect the term multiplied by $\sin\theta$ and arrive at:

$$\partial_r W = 0. \tag{51}$$

Second-order accurate numerical implementation is readily achieved by applying (51) at the grid-point $\left(i,\ J - \frac{1}{2}\right)$, obtaining $\partial_r W|^{n+1}_{i,J-\frac{1}{2}} = 0$, and finally

$$W^{n+1}_{i,J} = W^{n+1}_{i,J-1}. \tag{52}$$

In terms of the field constituents, (52) is used for P and U. For V we may use (6a), since it involves derivatives solely in the ζ direction.

All in all, we have:

$$V_{i,J}^{n+1} = V_{i,J}^{n-1} + \gamma_\zeta \left(V_{i+1,J}^{n} - V_{i-1,J}^{n}\right) - (\gamma_\zeta/\tilde{c}_i^n)\left(P_{i+1,J}^{n} - P_{i-1,J}^{n}\right) \quad (53a)$$

$$U_{i,J}^{n+1} = U_{i,J-1}^{n+1} \quad (53b)$$

$$P_{i,J}^{n+1} = P_{i,J-1}^{n+1} \quad (53c)$$

4.3 Corner Points

At the corner points of the numerical grid boundary, both the ζ direction and r direction boundary conditions apply. Since the moving frame FDTD code is intended to track collimated PBs that propagate mainly in the ζ direction, we shall prefer the ζ direction boundary conditions over the r direction ones. Thus, at all corner points, we use the ζ direction boundary condition which applies at the specific corner point.

5. NUMERICAL RESULTS

5.1 Cylindrically Symmetric Pulsed Beams in free Space

5.1.1 Reference Solution

As a first test case we used the moving-window FDTD scheme in free space to track the exact wavepacket solution known as the "complex source pulsed beam" (CSPB) [5]. This solution has the globally exact expression

$$p(\mathbf{x}, t) = \mathrm{Re}\left\{ \frac{1}{4\pi s} \overset{+}{f}(\tau) \right\}, \quad (54)$$

Where $\tau = t - s(\mathbf{x})/c - \imath b/c$ and

$$s(\mathbf{x}) = \sqrt{r^2 + (z - \imath b)^2}, \quad \mathrm{Re}\, s \geq 0. \quad (55)$$

Here $\overset{+}{f}(t)$ is any analytic function, defined as the inverse Fourier transform of positive frequency part of a spectral function $\hat{f}(\omega)$, i.e.,

$$\overset{+}{f}(t) = \frac{1}{\pi} \int_0^\infty d\omega \hat{f}(\omega) e^{-\imath\omega t}, \quad \mathrm{Im}\, t \leq 0. \quad (56)$$

The parameter $b > 0$ defines the collimation distance of the wavepacket. A paraxial approximation for (54) is obtained if we note from (55) that $s \approx z - \imath b + \frac{r^2}{2(z-\imath b)}$ for $r \ll \sqrt{z^2 + b^2}$, giving

$$p \approx \mathrm{Re}\left\{ \frac{1}{4\pi(z-\imath b)} \overset{+}{f}\left(t - \frac{z}{c} - \frac{r^2}{2c(z-\imath b)} \right) \right\}. \tag{57}$$

Further properties of this solution are discussed in [5]. In particular it should be noted that this solution does not vanish exactly ahead of the wavefront, but it rather has a weak precursor, which however moves forward together with the wavepacket. The effect of this field on the numerical solution is clarified in Section 5.1.3 below.

Finally, the exact expressions for the longitudinal and radial velocities, $v_z \equiv v$ and $v_r \equiv u$, respectively, are obtained by inserting (54) into (1).

5.1.2 Numerical Examples

In the numerical examples below we use $c = c_0 = 1$ and $b = 1$, without loss of generality. Furthermore, noting that the expression in (54) is singular at the "source plane" $z = 0$ where s has a branch cut (see [5]) we shall only consider the domain $z > 0$.

We use, as examples, the following two different pulses:

$$\overset{+}{f}(t) = \overset{+}{\delta}(t - \imath T/2) = \frac{1}{\pi\imath(t - \imath T/2)}, \tag{58a}$$

and

$$\overset{+}{f}(t) = -A_2^{(2)}\,\overset{+}{\delta}(t - \imath T_2/2) = \frac{-2A_2}{\pi\imath(t - \imath T_2/2)^3}, \tag{58b}$$

where $A_2 = T_2^3/8T$ is a normalization constant used to bring the peaks of the $\overset{+}{\delta}^{(2)}$ pulse and of the $\overset{+}{\delta}$ pulse to the same value. For the analytic δ function, denoted in (58a) as $\overset{+}{\delta}$, the parameter T is identified as the 3 dB temporal pulse width. The half-amplitude beamwidth obtained by using this function in (54) is found to be $W = W_0\sqrt{1 + (z/b)^2}$, with $W_0 = 2\sqrt{cTb}$ being the beamwidth at the waist $z = 0$ [5]. This pulse has a relatively slow axial decay and thus generates a less localized PB. It is therefore used here to study the interaction of the PB field with the numerical grid boundaries.

The twice differentiated analytic δ pulse $\overset{+}{\delta}{}^{(2)}$ in (58b) is a much more localized wavepacket that has less interaction with the boundaries (see numerical result below). For this pulse we have chosen the parameter T_2 to be 5 times larger than the parameter T used for the $\overset{+}{\delta}$ PB, in order to obtain similar wavepacket shapes near the pulse center.

Figures 2 and 3 show the results of numerical runs with $\overset{+}{\delta}$ and $\overset{+(2)}{\delta}$, respectively. The initial data for these runs were taken from the exact solution in (54) and was calculated at $t = 0.03$ to avoid the singularity of the exact solution at $z = 0$. The figures show snapshots of the field distributions at an early time when the PB is still in the near zone, at an intermediate time $(t = b/c)$ when the PB is in the Fresnel distance $z = b$, and at a late time $(t = 4b/c)$ when the PB is in the far zone $z = 4b$. The late time for $\overset{+}{\delta}$ corresponds to 2000 pulse lengths, or 20000 time steps. Examples with propagation length extending to order of 10^4 pulse lengths have also been worked out. In Figs. 2(d) and 3(d), which compare the numerical and the exact solutions, it is noticeable that the numerical solution for $\overset{+}{\delta}{}^{(2)}$ is more accurate than the numerical solution for $\overset{+}{\delta}$, especially near the front boundary. This phenomenon is due to the more compact form of the $\overset{+(2)}{\delta}$ PB which decays faster away from the pulse center, as explained in paragraph 5.1.3 below.

5.1.3 Analysis of Error Sources at the front Boundary

The boundary condition in (47) is based on the assumption that the size of the numerical grid has been chosen so that in the continuous (physical) realm there is no field ahead of the window. If, however, this assumption is not satisfied, the portion of the field ahead of the window will ultimately affect the field in the window. This would happen because the z-directed velocity component of the spectral constituents that propagate in off-axis directions is smaller than the propagation speed of the moving window. In view of the boundary condition in (47), these field constituents cannot be modeled by our numerical scheme.

This source of error is identified and studied in Figures 2–4. As mentioned after (57), our reference PB solutions do not vanish ahead of the wavefront, but rather have a weak precursor, which is stronger for

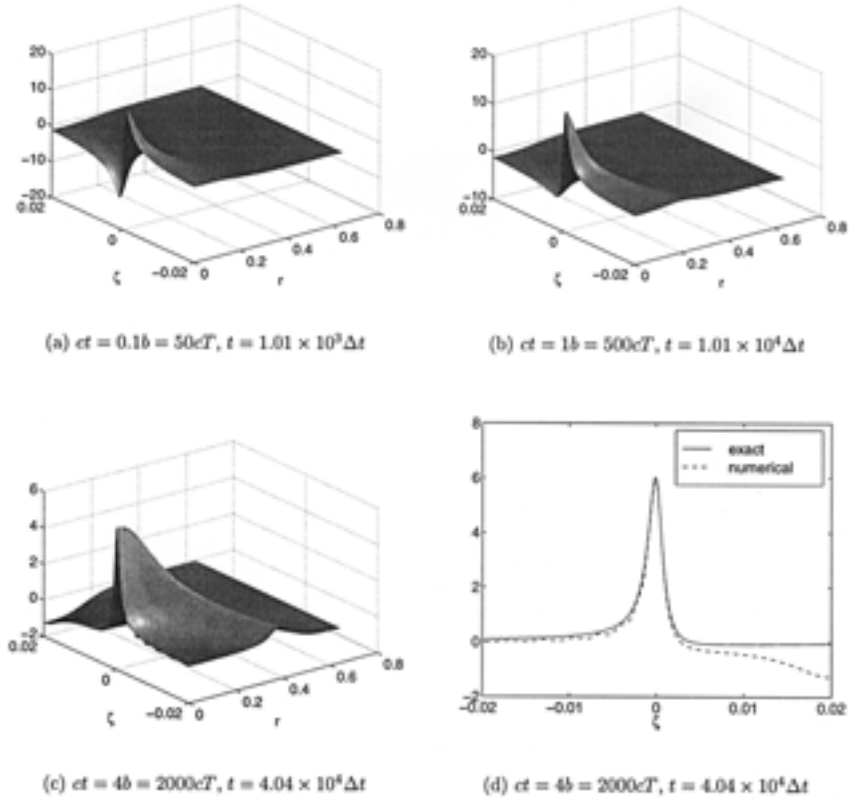

Figure 2. Numerical P field distribution in free space of a $\overset{+}{\delta}$ PB, shown at different propagation distances and times. The results where calculated using the cylindrically symmetric code. Problem parameters: $c_0 = 1$, $T = 2 \times 10^{-3}$, $\Delta\zeta = 2 \times 10^{-4}$, $\Delta r = 8 \times 10^{-3}$, $\gamma_\zeta = 0.495$, $I = 200$ and $J = 80$. Boundary conditions where applied as discussed in Sec. 1, with removal speed $c_1 = 2$ (see Eq. (46)). (a) is in the near-zone, (b) is at the Fresnel distance and (c) is in the far-zone. (d) compares the far zone numerical and exact P-field solutions along the PB axis (i.e., at $r = 0$). Note in particular the error at the front edge.

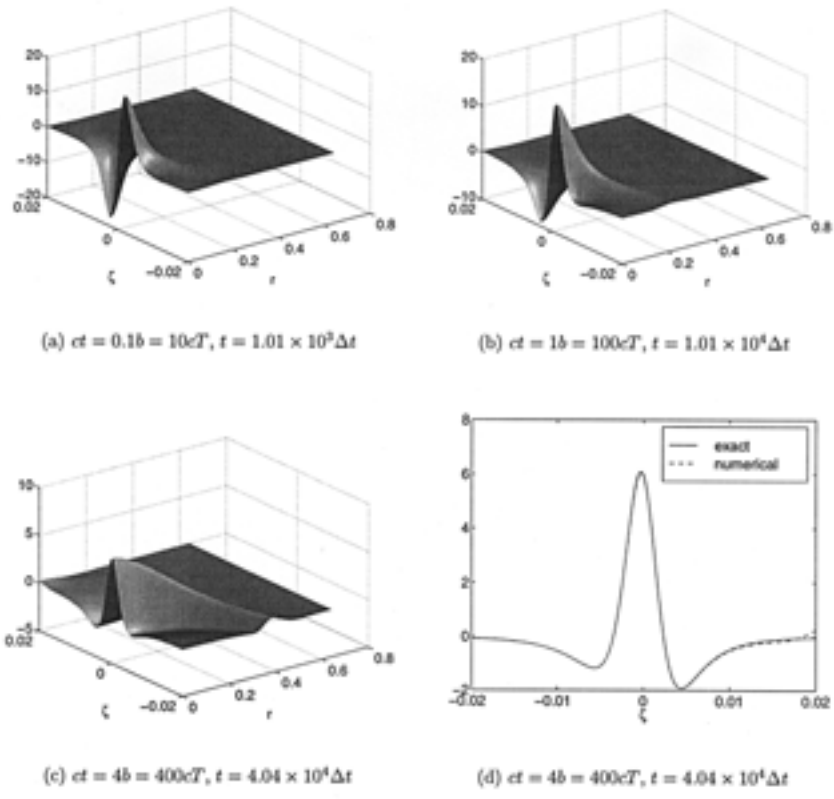

Figure 3. Same as Fig. 2 but for a $\overset{+}{\delta}{}^{(2)}$ PB in free space. All problem parameters are as in Fig. 2 except that here T is taken to be 10^{-2} in order to obtain a similar waveform to the one in Fig. 2.

the $\overset{+}{\delta}$ wavepacket and is weaker for the $\overset{+}{\delta}{}^{(2)}$ wavepacket (from (57) and (58) the axial decay for $|t - z/c| \gg T$ is governed by $(t - z/c)^{-1}$ for the former and by $(t - z/c)^{-3}$ for the latter). One readily observes that the numerical solution in Fig. 3(d) for $\overset{+}{\delta}{}^{(2)}$ is more accurate than the one in Fig. 2(d) for $\overset{+}{\delta}$, especially near the front boundary. The effect of the part of the physical solution that remains ahead of the moving window is studied in Figure 4 where numerical solutions attained from different sizes of the numerical window are compared to the exact solution (note that we have intentionally used the weakly-

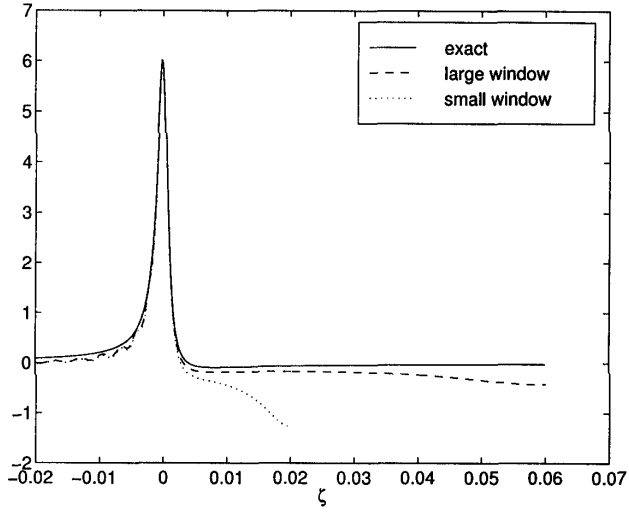

Figure 4. The effect of the numerical window size on the numerical solution. The figure compares the exact and numerical P field solutions along the PB axis (i.e., at $r = 0$). Two numerical window sizes are examined: The smaller window spans $0.02 \leq \zeta \leq 0.02$ with $I = 200$ (as in Fig. 2), while the large window spans $0.02 \leq \zeta \leq 0.06$ with $I = 400$. All other parameters are as in Fig. 2. Note that the window size affects only the error near the front boundary.

localized wavepacket defined by the $\overset{+}{\delta}$ signal). The numerical solution obtained for the wider window which encompasses a larger portion of the precursor is the most accurate since there are less field components ahead of the numerical window.

5.1.4 Removal of Reflected Wave Components from the back Boundary

Finally, in Fig. 5 we show the effect of c_1 from (42) on the numerical results for a $\overset{+}{\delta}$ CSPB at $ct = 4b$. It is interesting to note that higher values of c_1/c_0 than those shown also perform well and pose no numerical stability problems (the highest value attempted was $c_1/c_0 = 10^{10}$). There is no discernible difference between the numerical result for $c_1/c_0 = 10^{-1}$ and those obtained for higher values of c_1/c_0. Note in particular the results in Fig. 2(c) which were calculated using $c_1 = 2c_0$.

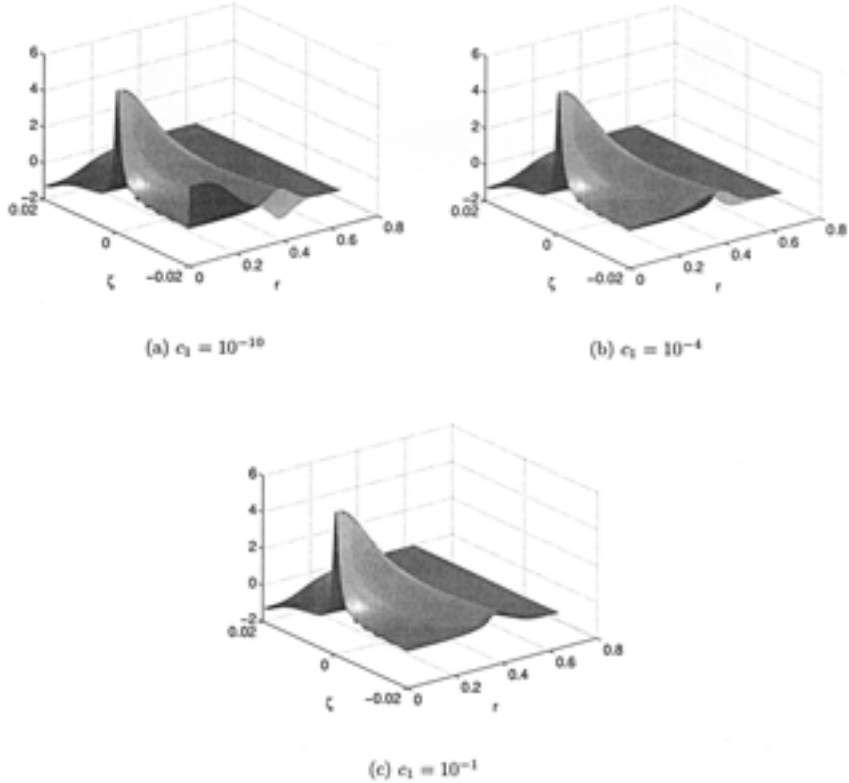

Figure 5. The effect of the removal speed c_1 on the numerical boundary conditions at the back boundary: The figure depicts numerical P field distributions of a $\overset{+}{\delta}$ PB in free space at $ct = 4b$, for different values of $c - 1$. All other problem parameters are as in Fig. 2. Note that case (c) in Fig. 2 which depicts the same P field distribution at the same time but with $c_1 = 2$ is indistinguishable from case (c) here.

5.2 Normal Propagation of Pulsed Beams in Plane Stratified Media

5.2.1 Reference Solution

A general expression for a PB field in a smoothly inhomogeneous medium has been given in [7]. In particular it has been shown that the PB propagation trajectory satisfies the ray equation. For the present problem of a PB normally impinging on a plane stratified medium the

propagation trajectory is a straight line along the stratification axis. Specializing the general solution in [7, Eq. (58)] to the present case (see details in Appendix A), we obtain

$$p(\mathbf{x},t) = \mathrm{Re}\left\{ \frac{\sqrt{c(z)/c(0)}}{4\pi\left(\bar{z}(z) - \imath b\right)} \overset{+}{f}(\tau) \right\}. \tag{59}$$

where here

$$\tau = t - \bar{t}(z) - \frac{r^2}{2c(0)\left[\bar{z}(z) - \imath b\right]}, \tag{60}$$

$$\bar{z}(z) = \int_0^z \frac{c(z')}{c(0)} dz, \quad \bar{t}(z) = \int_0^z \frac{dz'}{c(z')} \tag{61}$$

and for convenience we remove the real part symbol. This PB solution remains collimated up to a distance z_F obtained by solving

$$\bar{z}\left(z_F\right) = b, \tag{62}$$

with the arrival time $t_F = \bar{t}(z_F)$. One may readily see that for a homogeneous medium Eq. (59) degenerates to the paraxial approximation for the CSPB (57). In the numerical examples below we set $c(z) = 1 + az$ where $a > 0$, giving $\bar{z}(z) = az^2/2 + z$, $\bar{t}(z) = \frac{1}{a}\ln(az+1)$, $z_F = \frac{1}{a}\left[\sqrt{1+2ab} - 1\right]$ and $t_F = \frac{1}{a}\ln\sqrt{1+2ab}$. Finally, the other vector components are found from (59) via (1).

5.2.2 Numerical Examples

We chose $a = 0.1$. For $\overset{+}{f}$ we used the same choices as in (58). Figure 6 shows the results of numerical runs with $\overset{+}{\delta}{}^{(2)}$, using initial data from (59) at $t = 0$. In Fig. 6(d) one observes a good agreement between the numerical result and the approximate analytical solution of (59), even at large distances.

5.3 Full 3D Catesian Code

Finally, we also generated a 3D moving window FDTD code which should be applied for an astigmatic PB. This code has basically the same features as the one for the cylindrically symmetric solutions described above. To test this code it is applied below for the exact

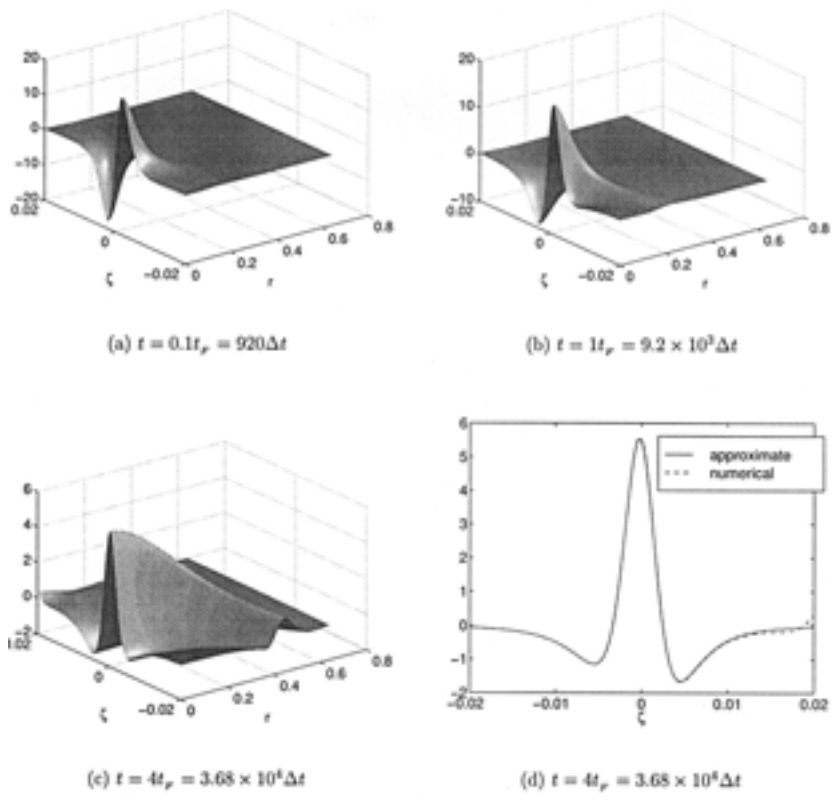

Figure 6. As in Fig. 3 but for a $\overset{+}{\delta}^{(2)}$ PB in a plane stratified medium $c(z) = 1 + az$ with $a = 0.1$.

stigmatic CSPB solution in free space described in Section 5.1. We also used the same choice of $\overset{+}{f}$ as in Section 5.1. Figure 7 shows the results of numerical runs with $\overset{+}{\delta}^{(2)}$ PBs at $ct = 4b$. To check the accuracy of the 3D numerical solution it is sampled at both the $y = 0$ and the $x = y$ planes, and the numerical solutions in the different planes are compared (we used spline interpolation for the result on the $y = x$ plane to match the spatial sampling of the solution in the $y = 0$ plane). The difference between the results in the different planes is very small, as can be seen in Fig. 7(c). This shows that the effect of the numerical dispersion in the different planes is almost identical.

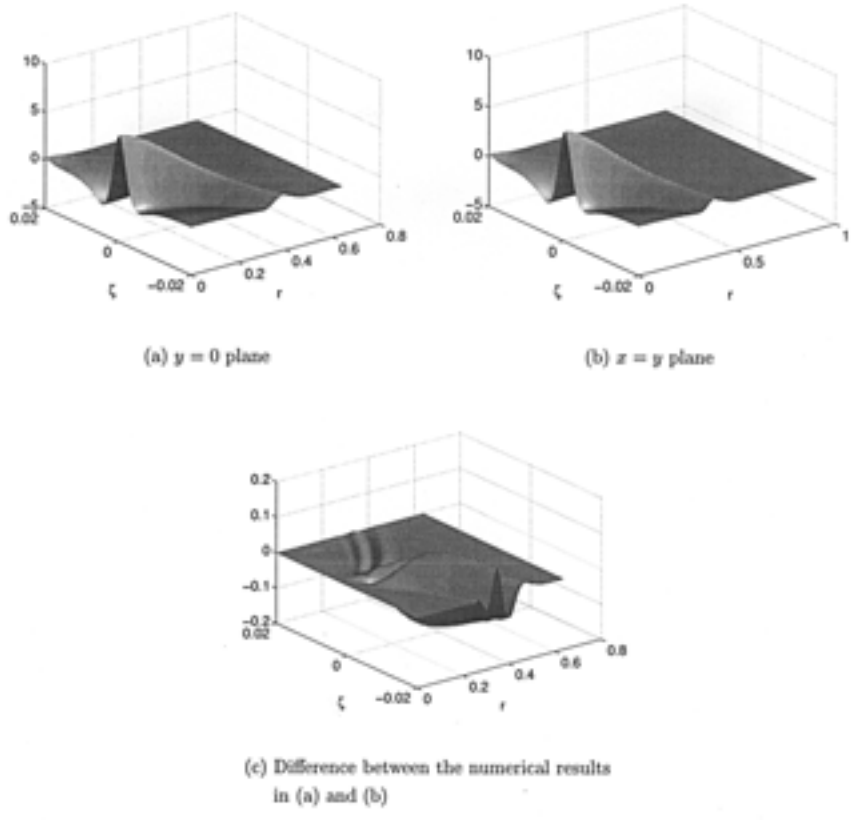

Figure 7. A study of the 3D FDTD code: The figure depicts the numerical P field distribution in free space of a cylindrically symmetric $\overset{+}{\delta}{}^{(2)}$ PB at $c_t = 4b$, obtained via a 3D FDTD solution. (a) shows the numerical solution in the $y = 0$ plane, (b) shows the numerical solution in the $x = y$ plane and (c) shows the difference between the solutions in (a) and (b). The numerical solution in the $x = y$ plane was interpolated (using splines) to match the spatial sampling of the numerical grid in the $y = 0$ plane. These results should be compared with case (c) in Fig. 3 which was calculated using the cylindrically symmetric code. All problem parameters are as in Fig. 3, except that here, instead of using $\Delta r = 8 \times 10^{-3}$ and $J = 80$, we use $\Delta x = \Delta y = 8 \times 10^{-3}$ with 80 sampling points in each direction.

6 CONCLUSIONS

It has been shown that modeling of long range propagation of collimated wavepackets, both in homogeneous and plane stratified media, is feasible using the moving frame FDTD approach. The distances modeled so far exceed the order of 10^4 pulse lengths. Obviously, a stationary frame formulation would be impractical for this size of problems. Our next goal is to develop the corresponding code for tracking wavepackets in more general 3D inhomogeneous media. To achieve this goal, we will have to construct a moving frame FDTD solver in a curvilinear coordinate system that is structured locally around the space-time ray trajectory that describes the wavepacket center of mass (this trajectory is calculated a priori using asymptotics; see [7]). Modeling of pulses along curved trajectories has already been demonstrated in [25], and initial steps have been taken towards incorporation of these tools into a 3D code along the lines discussed above. The problem of pulse propagation in a graded index waveguide, simulating structures such as fiber optics, is presented in another paper [18].

Appendix A. PB Solutions in Plane Stratified Media

The general solution for a PB in a smoothly varying medium is given in [7, Eq. (58)]. This solution is structured along a trajectory Σ satisfying the ray equation [7, Eq. (48)] whereon σ is an arc length. In these expressions $\mathbf{x} = (x_1,\ x_2)$ denote orthogonal coordinates transverse to σ as defined in [7, Eq. (39)], with $K(\sigma)$ and $k(\sigma)$ being the curvature and torsion coefficients along the ray trajectory.[2] The tensors $\mathbf{v_1}(\sigma)$ and $\mathbf{V_2}(\sigma)$ defined in [7, Eq. (46a)] measure the variations of the medium speed $v(\mathbf{r})$ normal to the ray trajectory. Finally, the solution in [7, Eq. (58)] is expressed in terms of the beam matrices $\mathbf{\Gamma}(\sigma)$, $\mathbf{P}(\sigma)$ and $\mathbf{Q}(\sigma)$ which are solutions of the matrix Riccati's equation [7, Eqs. (54, 55)] along Σ, subject to the initial conditions in [7, Eq. (56)], defined by the beamwidth and curvature of the generally astigmatic wavepacket at the initiation point.

In the present case, the medium is plane stratified and we note that $v(\mathbf{r}) = c(z)$. Since the PB impinges on the medium along the

[2] This appendix utilizes the notations of [7], using $\mathbf{r}$ for points in a 3D coordinate frame, $\mathbf{x}$ for the 2D coordinate transverse to Σ and $v(\mathbf{r})$ instead of c for the medium wavespeed.

stratification axis, its propagation ray trajectory is a straight line that can be taken to be along the z axis, with the $\mathbf{x}$ coordinates being the cartesian (x, y) coordinates. Noting that here $\mathbf{V_2} = 0$ we find from [7, Eq. (54–56)] that $\mathbf{Q}$ satisfies the equation $\mathbf{Q}' = c(z)\mathbf{I}$ with $\mathbf{Q}(0) = [\mathbf{\Gamma}(0)]^{-1}$, where $\mathbf{I}$ is the identity matrix, whose solution is $\mathbf{Q}(z) = [\mathbf{\Gamma}(0)]^{-1} + \mathbf{I}\int_0^z c(z')dz'$. The matrix $\mathbf{\Gamma}$ is finally found from $\mathbf{\Gamma}(z) = [\mathbf{Q}(z)]^{-1}$. For the present problem of a stigmatic PB with waist at the $z = 0$ plane and collimation distance b we choose $\mathbf{\Gamma}(0) = \imath(bc(0))^{-1}\mathbf{I}$, and thus

$$\mathbf{\Gamma}(z) = \mathbf{I}\left[\int_0^z c(z')dz' - \imath bc(0)\right]^{-1}. \tag{63}$$

Finally, substituting (63) into the the general solution in [7, Eq. (58)] we obtain the solution in (59).

REFERENCES

1. Brittingham, J. N., "Focus wave modes in homogeneous Maxwell's equations: Transverse electric mode," *J. Appl. Phys.,* Vol. 54, 1179–1189, 1983.
2. Ziolkowski, R. W., "Exact solutions of the wave equation with complex locations," *J. Math. Phys.,* Vol. 26, 861–863, 1985.
3. Besieris, I. M., A. M. Shaarawi, and R. W. Ziolkowski, "A bidirectional traveling plane wave representation of exact solutions of the scalar wave equation," *J. Math. Phys.,* Vol. 30, 1254–1269, 1989.
4. Moses, H. E., and R. T. Prosser, "Acoustic and electromagnetic bullets. New exact solutions of the acoustic and Maxwell's equation," *SIAM J. Appl. Math.,* Vol. 50, 1325–1340, 1990.
5. Heyman, E., and L.B. Felsen, "Complex-source pulsed-beam fields," *J. Opt. Soc. Am. A,* Vol. 6, No. 6, 806–816, 1989.
6. Heyman, E., B. Z. Steinberg, and R. Ianconescu, "Electromagnetic complex source pulsed beam fields," *IEEE Trans. Antennas Propagat.,* Vol. AP-38, 957–963, 1990.
7. Heyman, E., "Pulsed beam propagation in inhomogeneous medium," *IEEE Trans. Antennas Propagat.,* Vol. 42, 311–319, 1994.
8. Yee, K. S., "Numerical solution of initial boundary value problems involving Maxwell's equations in isotropic media," *IEEE Trans. Antennas Propagat.,* Vol. AP-14, 302–307, 1966.
9. Taflove, A., *Computational Electrodynamics, The Finite Difference Time-Domain Method,* Artech House, Boston, 1995.

10. Shlager, K. L., and J. B. Schneider, "A selective survey of the finite-difference time-domain literature," *IEEE Antennas Propagat. Magazine,* Vol. 37, No. 4, 39–56, 1995.
11. Engquist, B., and A. Majda, "Absorbing boundary conditions for the numerical simulation of waves," *Mathematics of Computation,* Vol. 31, 629–651, 1977.
12. Mur, G., "Absorbing boundary conditions for the finite-difference approximation of the time-domain electromagnetic-field equations," *IEEE Trans. Electromagnetic Compatibility,* Vol. 23, 377–382, 1989.
13. Higdon, R. L., "Absorbing boundary conditions for difference approximations to the multi-dimensional wave equation," *Mathematics of Computation,* Vol. 47, 437–459, 1986.
14. Higdon, R. L., "Numerical absorbing boundary conditions for the wave equation," *Mathematics of Computation,* Vol. 49, 65–90, 1987.
15. Fidel, B., E. Heyman, R. Kastner, and R. W. Ziolkowski, "Hybrid ray-FDTD moving window approach to pulse propagation," *Proc. of the 1994 International IEEE/AP-S Symposium,* 1414–1417, Seattle, WA, 1994.
16. Fidel, B., E. Heyman, R. Kastner, and R. W. Ziolkowski, "Hybrid ray-FDTD moving frame approach to pulse propagation," *J. Comp. Phys.,* Vol. 138, 480–500, 1997.
17. Hile, C. V., and W. L. Kath, "Numerical solutions of Maxwell's equations for nonlinear-optical pulse propagation," *J. Opt. Soc. Am. B,* Vol. 13, No. 6, 1135–1145, 1996.
18. Pemper, Y., E. Heyman, R. Kastner, and R. W. Ziolkowski "Hybrid ray-FDTD moving coordinate frame approach for long range tracking of pulsed fields in graded index waveguides," *J. Electromagnetic Waves and Applications,* Vol. AP-38, 957–963, 1990.
19. Lee, D., and A. D. Pierce, "Parabolic equation development in recent decade," *J. Comput. Aconst.,* Vol. 3, No. 2, 95–173, 1995.
20. Jensen, F. B., W. A. Kuperman, M. B. Porter, and H. Schmidt, *Computational Ocean Acoustics,* AIP Press, Woodbury, NY, 1994.
21. Murphy, J. E., "Finite-difference treatment of a time-domain parabolic equation: Theory," *J. Acoust. Soc. Am.,* Vol. 77, No. 5, 1406–1417, 1985.
22. Masoudi, H. M., and J. M. Arnold, "Parallel beam propagation methods," *IEEE Photon. Technol. Lett.,* Vol. 6, No. 7, 848–850, 1994.

23. Masoudi, H. M., and J. M. Arnold, "Parallel beam propagation method for the analysis of second harmonic generation," *IEEE Photon. Technol. Lett.,* Vol. 7, No. 4, 400–402, 1995.
24. McDonald, B. E., and W. A. Kuperman, "Time domain formulation for pulse propagation including nonlinear behavior at a caustic," *J. Aconst. Soc. Am.,* Vol. 81, No. 5, 1406–1417, 1987.
25. Aloni, E., R. Kastner, E. Heyman, and R. W. Ziolkowski, "Reduction of numerical dispersion errors in the FDTD with multiple moving coordinate systems," *URSI Meeting,* Baltimore, MD, July 21–26, 1996.